Automatic trajectory control of single cells using dielectrophoresis based on visual feedback

Alexis Lefevre, Michaël Gauthier, Pauline Bourgeois, Annie Frelet Barrand, Aude Bolopion

Journal Name

ARTICLE TYPE

Cite this: DOI: 00.0000/xxxxxxxxxx

Automatic trajectory control of single cells using dielectrophoresis based on visual feedback†

Alexis Lefevre, Michaël Gauthier, Pauline Bourgeois, Annie Frelet-Barrand and Aude Bolopion

Received Date
Accepted Date

DOI: 00.0000/xxxxxxxxxx

Abstract

This paper deals with the automatic control of the trajectory of T-lymphocytes using dielectrophoretic (DEP) actuation. Dielectrophoresis is a physical phenomenon induced by a non uniform electric field enabling to apply a force on a dielectric object. In most of the cases, it is used in a passive way. The electric field is in a steady state and the force applied on the cells depend on the cell's characteristics and position inside the channel. Those systems are limited as cells with similar characteristics will undergo the same forces. To overcome this issue, active devices where the electric field changes over time were developed. However, the voltages that should be applied to generate the desired electric field are mostly computed offline using finite element methods. Thus, there is a low number of devices using automatic approaches with dielectrophoretic actuation where the electric field is computed and updated in real-time based on the current position of the cell. We propose here an experimental bench used to study the automatic trajectory control of cells by dielectrophoresis. The computation of the dielectrophoretic force is done online with a model based on the Fourier series depending on the cell's characteristics, position and electric field. This model allows the use of a controller based on visual feedback running at 120 Hz to control the position of cells inside a microfluidic chip. As cells are sensitive to electric field, the controller is limiting the norm of the electric field while maximizing the gradient to maximize the DEP force. Experiments have been performed and T-lymphocytes were successfully steered along several types of trajectories at a speed of five times their size per second. The mean error along those trajectories is below $2\,\mu$m. The viability of the cells has been checked after the experiments and confirms that this active DEP actuation is not harming the cells.

1 Introduction

Single cell motion control has recently gained interest as the study of specific biological behaviors needs the monitoring and acting capabilities at the scale of a single cell[1,2].

The classical way to displace individual cells relies on methods where the cell is mechanically handled[3]. The use of micropipette is common, the negative pressure created inside the pipette is used to hold the cell. This principle is extended to study cell's mechanical properties or interactions[4]. However, those types of positioning cannot be performed in closed environments, thus recent studies focused on the use of cell positioning without contact. Non-contact positioning can be classified in two categories, if an intermediate device is used or not. The indirect positioning refers to methods[5,6], where a physical principal (e.g. magnetic field) is used to actuate an intermediate tool able to handle cells. The direct non-contact positioning refers to methods where the cell itself is directly influenced by the physical phenomenon. The most commonly used physical principles are acoustic waves[7,8], optical tweezers[9,10] and electric fields[11,12]. Each technics has advantages and drawbacks [2,13]. This article focuses on electric fields which are particularly interesting as they can induce fluid flows by electro-osmosis or electro-thermal effects[14], be used to characterize cells[15] and displace cells with dielectrophoresis[16]. The displacement of cells using dielectrophoresis is actively studied. Most of the works consist of sorting cells inside a micro-channel using a steady electric field and rely on the differences between cells characteristics to achieve the separation[11]. A more advanced platform has been developed by Godino et al.[17] where they use a visual feedback to track the position of cells and switch on/off the voltage on electrodes to generate or not dielectrophoretic forces on the cell. It results in a device that is used to study cells and cell interaction. The DEPArray™[18], allowing to retrieve specific cells inside a sample with low concentration, is recently used in several publications[19–21] for cell analysis despite its limited

All authors are with Université de FrancheComté,CNRS, SUPMICROTECH, Institute FEMTO-ST, F25000 Besançon, France

† Electronic Supplementary Information (ESI) available: [Two figures adding information about the model used in this article. One figure showing the necessity of transparent electrodes. One figure showing the result of a simulation assessing the performance of the proposed closed-loop controller. A video showing the camera view during an experiment.]. See DOI: 00.0000/00000000.

throughput. However, the control of cell's trajectory using dielectrophoresis is an ongoing work. Several studies and experimental platforms[22–24] have been built to steer artificial objects along a defined trajectory, however, the demonstration on biological objects remains a challenge addressed in this paper.

This article deals with an experimental platform to perform trajectory control of cells based on visual feed-back using dielectrophoresis inside a PDMS pool. In our previous work we demonstrated the effectiveness of our model based on Fourier series to compute the dielectrophoretic force[25] and of our controller, allowing to steer microbeads along a defined trajectory[26]. However, the cells behave differently from microbeads as both have different density and different sensitivity to electric fields (beads may experience large electric field and cells cannot). Thus, the controller developed for microbeads cannot be used on cells. We consequently propose a new controller for cell motion control based on visual feedback. Successful trajectory control of T-lymphocytes are realized following different paths and viability tests confirm that the cells are not perturbed by the controller.

The rest of this paper is organized as follows. Section 2 describes the dynamic model. Section 3 defines the open loop controller which is a first step to build the closed-loop controller presented in section 4. The description of the experimental is given in section 5 and experimental results and discussion are detailed in section 6. Finally, section 7 concludes the paper.

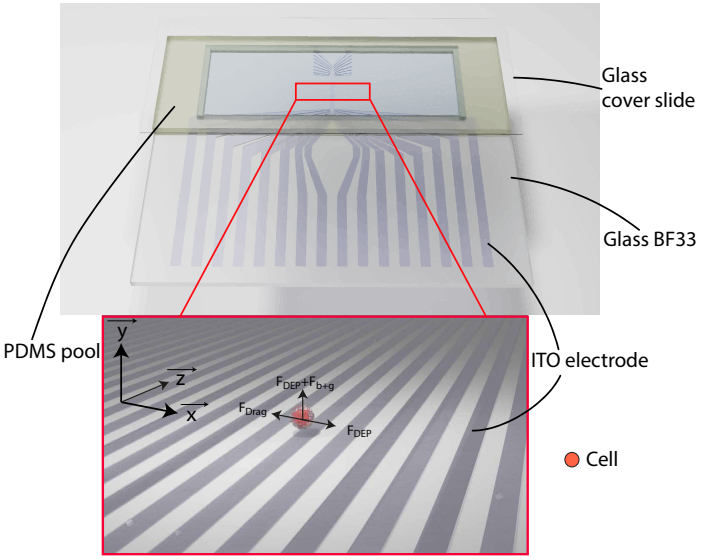

Fig. 1 Representation of the system, and schematics of the working area from a top view. It defines the orientation of $\vec{x}$ axis that is perpendicular to the electrodes, $\vec{y}$ axis that is the axis of the altitude, and $\vec{z}$ axis which is parallel to the electrodes. The three main forces undergone by the cell, $\mathbf{F}_{DEP}$, $\mathbf{F}_{Drag}$ and $\mathbf{F}_{b+g}$, are represented. The chip is composed of transparent electrodes made of ITO (Indium Thin Oxyde) on top of glass BF33 (Borofloat).

2 Model definition

This section is based on the models that have been used in[26] to compute the dominating forces applied on the cell. The system is a microfluidic chip composed of parallel electrodes independently supplied in voltages. Those electrodes are used to generate a dielectrophoretic force in the $(\vec{x},\vec{y})$ plan inducing a displacement of the cell in the same plan. The Fig. 1 shows the chip and defines the orientation of the used axis. It also represents the forces applied on the cell and an overview of the chip which will be introduced more deeply in section 5. The next parts of the section defines the model of the cell and the computation of the considered forces.

2.1 Cell model

The model used for the cell is the "Single shell model" presented by Sukhorukov et al.[27]. Following this model the cell is considered as a spherical particle composed of an intern part covered by a uniform shell. The characteristics of each part are used to create an equivalence of the cell in terms of electrical behavior characterized by a conductivity and permittivity σ_c and ε_c. This electrical model is needed to compute the Clausius-Mossotti factor K that characterizes the difference of polarizability between the medium, of conductivity σ_m and permittivity ε_m, and the cell. The dielectrophoretic force is proportional to the Clausius-Mossotti factor, the sign of this factor also determines if the cell undergoes positive or negative dielectrophoresis. The software MyDep[28] and its database are used to compute the Clausius-Mossotti factor depending on the frequency. Considering human T-cells in a medium with $\sigma_m = 0.2\mathrm{S\,m^{-1}}$, it reveals that to perform negative dielectrophoresis the used frequency must be $f_{hz} \leq 50\,\mathrm{kHz}$. Moreover, it has been shown by Napotkin et al.[29] that cells are sensitive to the potential across their membrane V_{tm} called transmembrane potential. If V_{tm} exceeds 200 mV, the cells can be damaged due to electroporation. The potential that cross the membrane is defined[30] as:

$$V_{tm} = \frac{1.5Ea}{\sqrt{1+(\omega\tau)^2}}, \quad \tau = \frac{RC_{mem}(\sigma_{cyto}+1/2\sigma_m)}{1+R\sigma_{mem}(\sigma_{cyto}+1/2\sigma_m)} \tag{1}$$

where E is the electric field norm, a the cell radius, ω the frequency of the applied voltage, C_{mem} the capacitance of the cell membrane, σ_{cyto} is the cytoplasmic conductivity, σ_m is the conductivity of the medium, and σ_{mem} is the membrane conductivity. Considering a human T-cell of $10\,\mu$m of diameter and a medium with $\sigma_m = 0.2\mathrm{S\,m^{-1}}$, the electric field must not exceed $|\mathbf{E}_{max}| = 26668\,\mathrm{V\,m^{-1}}$ to not affect the cell (Fig. S1 in supplementary materials). $|\mathbf{E}_{max}| = 25000\,\mathrm{V\,m^{-1}}$ is retained for the following. This model will be used in the rest of this article. The next part defines the forces undergone by a cell during its displacement inside the chip.

2.2 Equation of motion

The equation of motion comes from Newton's second law and depends on the main forces at stake. The considered forces are the fluid drag force $\mathbf{F}_{drag}$, the gravity-buoyancy $\mathbf{F}_{g+b}$ and the dielectrophoretic force $\mathbf{F}_{DEP}$. The AC electro-osmosis, Brownian motion and electro-thermal flow are at least two orders of magnitude less than the dielectrophoretic force[31] and are consequently

neglected. Kharboutly *et al.*[32] demonstrated that the inertial term in Newton's second law can be neglected at this scale for spherical particles. As a result, the equation of motion is:

$$\begin{bmatrix}0\\0\end{bmatrix} = \mathbf{F}_{g+b} + \mathbf{F}_{drag} + \mathbf{F}_{DEP} \tag{2}$$

2.2.1 Definition of $\mathbf{F}_{g+b}$

$\mathbf{F}_{g+b}$ is the combination of the gravity and buoyancy forces describes by:

$$\mathbf{F}_g = \begin{bmatrix}0\\ \frac{4}{3}\pi a^3(\rho_m - \rho_p)g\end{bmatrix} \tag{3}$$

where a is the radius of the particle, ρ_m (resp ρ_p) is the fluid density (resp. particle density) and g is the gravitational acceleration.

2.2.2 Definition of $\mathbf{F}_{drag}$

$\mathbf{F}_{drag}$ is the drag force. It takes into account the effect of the floor of the chip[33,34] resulting in :

$$\mathbf{F}_{drag} = -6\pi\mu a \begin{bmatrix}\lambda_x & 0\\ 0 & \lambda_y\end{bmatrix} \cdot \begin{bmatrix}\dot{x}\\ \dot{y}\end{bmatrix} \tag{4}$$

where μ is the dynamic viscosity, $\dot{x}$ (resp $\dot{y}$) is the particle velocity on the $\vec{x}$ (resp $\vec{y}$) direction. λ_x and λ_y are correction factors[31] and enable to model the impact of the substrate when the cell is close to it. They are defined as:

$$\lambda_x = \left[1 - \frac{9}{16}\frac{a}{y} + \frac{1}{8}\left(\frac{a}{y}\right)^3\right]^{-1}, \tag{5}$$

$$\lambda_y = \frac{8}{15}\sinh\alpha\left[\frac{2\sinh 3\alpha + 3\sinh 2\alpha}{4\sinh^2 1.5\alpha - 9\sinh^2\alpha} - 1\right] \tag{6}$$

where

$$\alpha = \cosh^{-1}(1 + (y-a)/a)$$

with y the altitude of the center of gravity of the particle above the substrate.

2.2.3 Definition of $\mathbf{F}_{DEP}$

$\mathbf{F}_{DEP}$ is the dielectrophoretic force. It depends on the gradient of the square of the electric field generated by the electrodes. The computation of this force need to be fast enough to be used in the closed-loop controller. The used model, referred as FSM, was developed[25] by Gauthier *et al.* It considers that inside a homogenous medium, for dielectrophoretic applications, the potential is defined by the Laplace's equation Eq. 7:

$$\vec{\nabla}^2\phi = 0 \tag{7}$$

This equation states that the permittivity and conductivity have no impact on the electric field. In addition, the laplacian is a linear operator which allows to consider the potential generated by all the electrodes as a linear combination of the contribution of each electrode. The FSM model assumes that this linear combination can be expressed as a Fourier series. This assumption is verified by the convergence of the found Fourier series[25,35]

The expression of the potential using the FSM is:

$$\phi(x,y,\mathbf{U}(t)) = \mathbf{e}(x,y)^T \cdot \mathbf{A} \cdot \mathbf{U}, \tag{8}$$

where $\mathbf{e}(x,y)$ is a sum of exponential terms[25]. $\mathbf{A}$ is a matrix composed of the Fourier series coefficients and $\mathbf{U}$ is a vector composed of the potential applied on each electrode.

The electric field $\mathbf{E}$, generated by the electrodes, can be expressed as:

$$\mathbf{E} = -\vec{\nabla}(\phi) = -\begin{bmatrix}\frac{\partial \mathbf{e}^T}{\partial x}\mathbf{A}\mathbf{U}\\ \frac{\partial \mathbf{e}^T}{\partial y}\mathbf{A}\mathbf{U}\end{bmatrix} \tag{9}$$

and

$$\mathbf{F}_{DEP} = C_{DEP}\begin{bmatrix}E_x\frac{\partial E_x}{\partial x} + E_y\frac{\partial E_x}{\partial y}\\ E_x\frac{\partial E_y}{\partial x} + E_y\frac{\partial E_y}{\partial y}\end{bmatrix} \tag{10}$$

inducing

$$\mathbf{F}_{DEP} = C_{DEP}\begin{bmatrix}\frac{\partial^2 \mathbf{e}^T}{\partial x^2}\mathbf{A}\mathbf{U} & \frac{\partial^2 \mathbf{e}^T}{\partial x \partial y}\mathbf{A}\mathbf{U}\\ \frac{\partial^2 \mathbf{e}^T}{\partial y \partial x}\mathbf{A}\mathbf{U} & \frac{\partial^2 \mathbf{e}^T}{\partial y^2}\mathbf{A}\mathbf{U}\end{bmatrix} \cdot \begin{bmatrix}\frac{\partial \mathbf{e}^T}{\partial x}\mathbf{A}\mathbf{U}\\ \frac{\partial \mathbf{e}^T}{\partial y}\mathbf{A}\mathbf{U}\end{bmatrix} \tag{11}$$

with $C_{DEP} = 4\pi\varepsilon_m a^3 K$ and K the Clausius-Mossotti factor. This formulation is suited to compute the dielectrophoretic force from the electric potential field as the derivatives of exponential terms are relatively easy to compute. In addition, the last expression can be rewritten as:

$$\mathbf{F}_{DEP} = \mathbf{U}(t) \cdot \mathbf{P} \cdot \mathbf{U}^T \tag{12}$$

where:

$$\mathbf{P} = C_{DEP} \cdot \left(\frac{\partial \mathbf{e}^T}{\partial \mathbf{X}}(x,y) \cdot \mathbf{A}\right)^T \cdot \frac{\partial^2 \mathbf{e}^T}{\partial \mathbf{X}^2}(x,y) \cdot \mathbf{A} \tag{13}$$

with $\mathbf{X} = \begin{bmatrix}x\\ y\end{bmatrix}$. Equation 12 shows that this method allows to decouple the command variable $\mathbf{U}$ from the other variables making this model interesting for closed-loop control where $\mathbf{U}$ has to be computed several times per second. In the next part, the precision of the FSM compared to FEM simulation is discussed.

2.3 Precision regarding the electric field

The ability of the FSM to compute dielectrophoretic force has already been compared with classical FEM using the COMSOL Multiphysics® software[26]. For this application, it is interesting to compare the FSM regarding the norm of the electric field as it is a key parameter to avoid cell damage, as seen in section 2.1. For these simulations the properties of the medium are σ_m =0.2 S m^{-1} and ε_m =78 The electrodes are considered with a negligible thickness. The simulated chip is composed of 16 electrodes with a width of 10 μm and a gap between two electrodes of 10 μm. The boundary conditions are defined in[26]. One electrode is supplied with 5 V and the others are all at 0 V. It results that close to the supplied electrodes and below 5 μm the difference is between -20% and 20%. However, as the considered cell has a diameter of 10 μm, 5 μm is the minimum possible altitude of the cell. Above

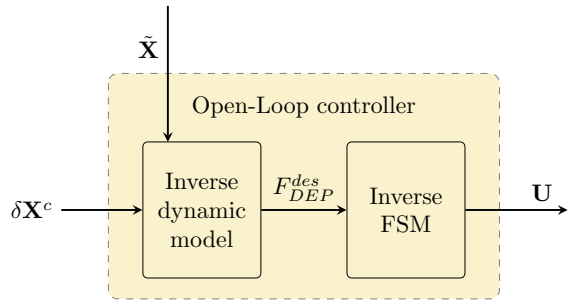

Fig. 2 Block diagram of the open-loop controller. The inputs are the desired displacement $\delta\mathbf{X}^c$ and the estimated position of the cell $\tilde{\mathbf{X}}$. This information fed the inverse dynamic model that computes $\mathbf{F}_{b+g}$ and $\mathbf{F}_{drag}$ and outputs the desired DEP force $\mathbf{F}_{DEP}^{des}$. Based on $\mathbf{F}_{DEP}^{des}$, the inverted FSM computes $\mathbf{U}$, the set of voltages that is applied on the physical system to induce a displacement $\delta\mathbf{X}^c$ to the cell.

$5\,\mu$m and up to the substrate, the FSM is always overestimating the norm of the electric field (Fig. S2 in supplementary materials). This guaranties that the electric field computing by the FSM is relevant information that can be controlled to avoid the phenomenon of electroporation described in section 2.1. The next section is about the definition and precision of the open-loop controller.

3 Open-loop controller

The open-loop controller consists in controlling the voltage applied on each electrode to move the cell to a desired position. It is based on the model of the previous section. With this model it is possible to compute the displacement of a cell knowing its properties, the medium properties, the electrodes geometry and the applied voltage on each of them. The purpose of the open-loop controller is to solve the opposite problem, to compute the voltages $\mathbf{U}$ knowing the targeted displacement, the medium properties and the electrode geometry. The block diagram in Fig. 2 represents the controller composed of two parts. The first one, "Inverse dynamic model", takes as input the desired displacement and the position of the cell. It computes $\mathbf{F}_{b+g}$, $\mathbf{F}_{drag}$ and outputs the desired DEP force $\mathbf{F}_{DEP}^{des}$ that should be applied to perform the desired motion. The DEP force is fed in the inverse model of the FSM which outputs $\mathbf{U}$. This set of voltages is then applied to the physical system.
The inversion of the dynamic model is computed based on equation Eq. 3 and 4. The inversion of the FSM and the behavior of this controller are detailed in the following parts.

3.1 Inversion of the FSM

The inversion of the model consists in finding $\mathbf{U} \leq \mathbf{U}_{max}$ a set of voltages applied to the electrodes that induces a force $\mathbf{F}_{DEP}^{des}$ to the cell. $\mathbf{U}_{max}$ being the maximal voltage that can applied without damaging the electrodes. The considered chip is composed of $N_e = 16$ parallel electrodes. This geometry of electrodes and the non-linearity inherent to the dielectrophoretic force (Eq. 10) make the inversion of the model a problem with several outputs, redundancies and non-linearity which has no analytical solution. As shown in previous works[26], the simulated annealing is an efficient algorithm to invert the FSM. The simulated annealing is a stochastic algorithm used to approximate the global minimum of a function $f_{cost}(\mathbf{U}) = N_{rj}$, where N_{rj} is the energy of the system. This algorithm replicates the behavior of an annealing method. The system is considered with an initial virtual temperature T_{init} which decreases until T_{final} following $T = T_{init}\,e^{-t.\beta}$ with t the step number and β a coefficient allowing to control the number of iteration between T_{final} and $T = T_{init}$. At each step, the parameter of $f_{cost}(\mathbf{U})$ randomly changes and the energy is updated. If the new energy is lower than the previous one, it is saved and the algorithm goes to the next iteration. If the energy has increased the new solution is randomly saved depending on the value of T. This avoids getting stuck in local minimum and goes on until N_{rj} reached an arbitrary value called ε_{stop} or until $T < T_{final}$.

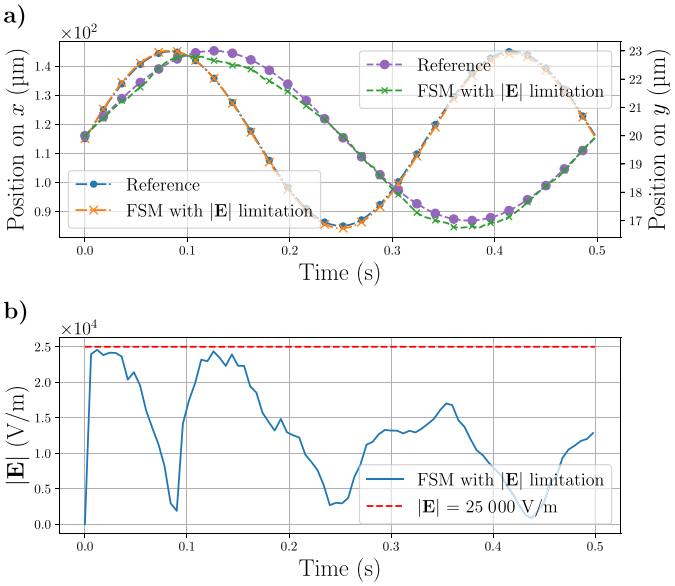

Fig. 3 Simulation of trajectory control of human T-cell at high speed using the open-loop controller. Figure a) represents the reference and followed trajectory on $\vec{x}$ and $\vec{y}$. The reference trajectory on $\vec{x}$ is a sinusoidal one with a maximum velocity of $375\,\mu\mathrm{m\,s}^{-1}$.The maximum error on both axis is below $4\,\mu$m. Figure b) shows that the limitation of electric field is effective as during all the experiment the curve never crosses the dashed line representing $|E|_{max}$ fixed here at $25\,000\,\mathrm{V\,m}^{-1}$.

For the inversion of the model, the parameter of the cost function is $\mathbf{U}$, the voltage applied on each electrode. As the objective is to find a $\mathbf{U}$ enabling to induce a desired DEP force to the cell, the force is used as a criterion for the optimization. The goal of the algorithm is to minimize the cost function representing the difference between the desired force and the one computed by the FMS as a function of $\mathbf{U}$. It also considers a limitation of the norm of the electric field in order to limit the maximum electric field at the location of the cell. The cost function is defined by:

$$f_{cost}(\mathbf{U}) = (\alpha_x \Delta F_x + \alpha_y \Delta F_y) - \varepsilon_{stop} + Flag_{|E|} \qquad (14)$$

where $\Delta F_x = F_x^{Des} - F_x(\mathbf{U})$ and $\Delta F_y = F_y^{Des} - F_y(\mathbf{U})$. $F_x(\mathbf{U})$ and $F_y(\mathbf{U})$ are the forces computed by the FSM generated by the set of voltages $\mathbf{U}$. α_x and α_y are the weights managing the importance of the error on the different axis. $Flag_{|E|}$ represents a penalty func-

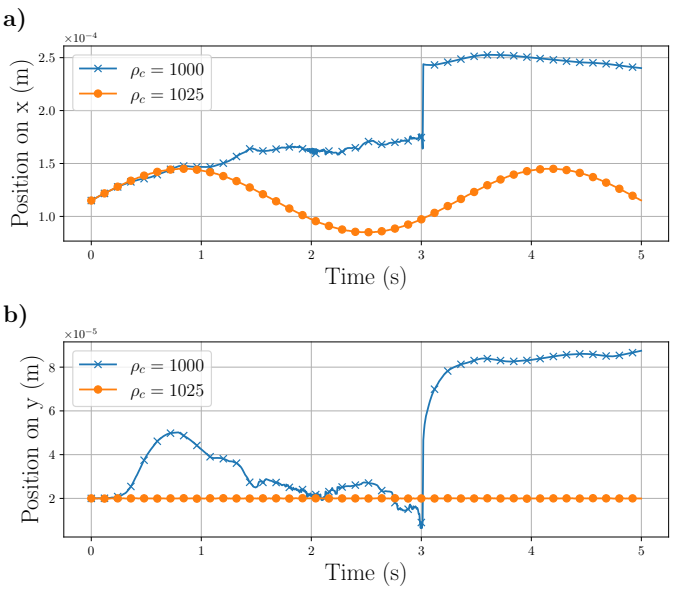

Fig. 4 Effect of the density of the object on the control. A set of voltages has been computed for a simulated cell of density $\rho_c = 1025$ to follow a sinusoidal path. The set of voltages is then applied to two simulated cells where the only difference is their density, one with $\rho_c = 1025$, another one with $\rho_c = 1000$. The top part of the figure represents the trajectory followed by the two simulated cells on $\vec{x}$ axis while the bottom part represents the trajectory on $\vec{y}$ axis. It shows that the control in open-loop is sensitive to the altitude and variation of density as the two curves quickly diverge.

tion of the value of the norm of the electric field $|E|$ applied to the cell compared to the maximum value $|E|_{max}$:

$$Flag_{|E|} = \begin{cases} 2.\varepsilon_{stop} & \text{if } |E| > |E|_{max} \\ 0 & \text{else} \end{cases} \quad (15)$$

This parameter ensures that the electric field applied to the cell does not exceed $|E|_{max}$, the one that damages the cell (section 2.1).

3.2 Simulation of trajectory control

The open-loop controller is implemented to realize simulation of trajectory control. For those simulations, the considered cell is a human T-cell defined in section 2.1 with $\rho_c = 1025$ and a radius $a = 5\,\mu$m. The simulation is running at 120 Hz to replicates experimental conditions. The chosen reference trajectories are sinusoidal ones on both $\vec{x}$ and $\vec{y}$ axis. The maximum speed on the $\vec{x}$ axis is of $375\,\mu\text{m}\,\text{s}^{-1}$ which should require high $|E|$. The results of a simulation are presented in Fig. 3. Fig. 3.a) represents the reference and followed trajectories on both axis. The maximum error is below $4\,\mu$m. Fig. 3.b) represents $|\mathbf{E}|$ at the location of the simulated cell. It shows that $|\mathbf{E}|$ never exceeds the limit $|\mathbf{E}_{max}| = 25000\,\text{V}\,\text{m}^{-1}$, meaning that the limitation of electric field is effective. The next section analyses the impact of an imprecision of the density of a cell on the open-loop controller.

3.3 Sensitivity to the density

The open loop controller presented here computes a set of voltages $\mathbf{U}$ to move a cell accordingly to a predefined trajectory. The previous section describes the behavior of the optimization algorithm used for this task and shows that this an iterative process computing the DEP force applied to the cell for each iteration. Section 2 shows that the DEP force is computed for one point in space and that its magnitude and direction is highly dependent of the position. Thus, a good knowledge of the position of the controlled cell is needed. While working with cells, the controller needs to be robust because of this heterogeneity in terms of size, shape and density. Simulations where conducted to demonstrate the sensitivity to this open loop controller to a wrong estimation of density and the results are presented in Fig. 4. One set of voltages was computed for an object with a density $\rho_c = 1025$ and applied in a simulated open-loop to two objects with respective density $\rho_c = 1025$ and $\rho_c = 1000$. For the object with $\rho_c = 1025$ the trajectory is the expected one, on the other hand, for the object $\rho_c = 1000$ the control is lost. The error on the density induces an error in the computation of $\mathbf{F}_{b+g}$ leading to an increase of the altitude of the object over time. The DEP force is computed at a wrong location as the estimated altitude is not the good one and the error is accumulating with time. Same observation can be done for a wrong estimation of the size of the object as $\mathbf{F}_{b+g}$ is also dependent of this parameter.

This section describes the principle of the open-loop controller and shows its sensitivity to parameters. It put forwards the importance of a closed-loop control to increase the robustness of the control regarding external perturbations and model approximations.

4 Closed-loop controller

The previous section defines the open-loop controller, which relies on the models but does not take into consideration the measured position of the cell. A closed-loop controller uses the same model with added feed-back information on the position of the cell on $\vec{x}$ and $\vec{y}$ axis. This information allows to compensate the imprecision of the model and external perturbations as well as the different size and shape of the cells that will induce a different motion.

4.1 Closed loop controller

The designed closed loop controller is based on visual feedback from a top view to obtain the position of the cell along the $\vec{x}$ axis. As the measurement of the altitude of a cell inside a pool is a tedious task that requires specific equipment, design and processing[36], it is proposed here to reconstruct the altitude using an observer. The observer corrects the estimated altitude of the cell by the FSM using the measured displacement of the cell on the $\vec{x}$ axis. The behavior of this controller is defined in Fig. 5. It takes as an input $\mathbf{X}^{des} = \begin{bmatrix} x^{des} & y^{des} \end{bmatrix}^T$ which represents the succession of positions that the cell has to follow. The measured error $\varepsilon = \begin{bmatrix} \varepsilon_x & \tilde{\varepsilon}_y \end{bmatrix}^T$ is computed using the measured value x^m and a corrected reconstruction of the altitude y^{corr} computed by an observer (called "$\tilde{y}$ Observer"), that will be detailed in a following section 4.1.1. A PI controller is then used to compute the com-

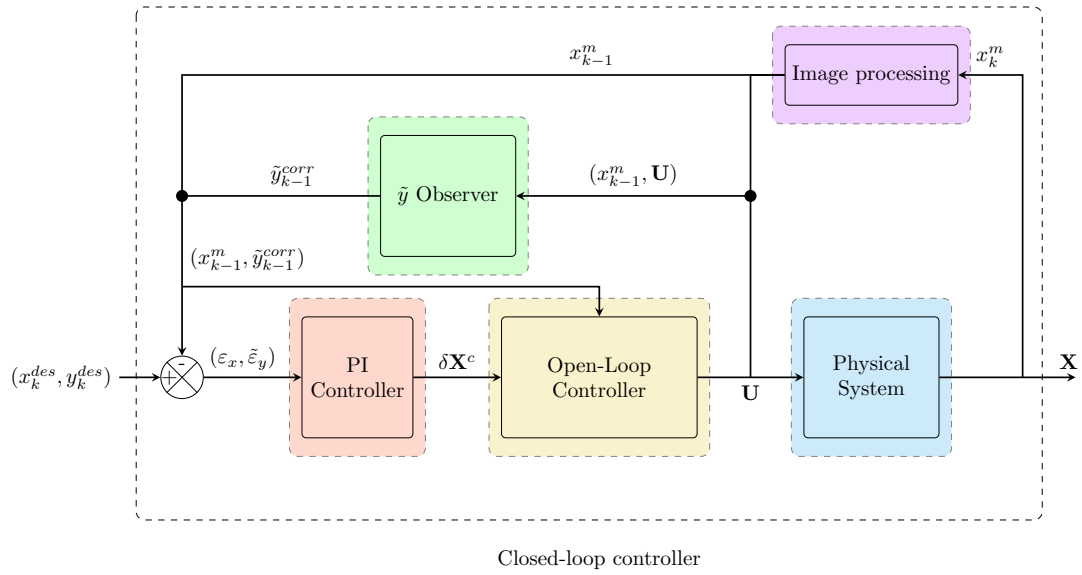

Fig. 5 Closed loop control architecture. The control purpose is to perform closed-loop actuation of cells based on visual feedback. It is composed of a PI controller, an open-loop controller, a direct model and an observer.

mand $\delta\mathbf{X}^c = \begin{bmatrix} \delta x^c \\ \delta y^c \end{bmatrix}$ that is used as an input for the "Open-Loop Controller" which was defined in the previous section. It outputs a vector of voltages $\mathbf{U}$ which is applied on the real system inducing the displacement of the cell which position x^m is recorded by a high speed camera.

The next paragraphs detail the behavior of the proposed altitude observer to obtain feedback information on $\vec{y}$ axis based on the image processing on $\vec{x}$ axis.

4.1.1 Behavior of the altitude observer

During the experiments, an error between the desired motion of the cell and the measured one will occur and is used to correct the estimated altitude. Indeed, if the estimated altitude is higher than the real one, the cell will undergo a higher DEP force inducing a bigger displacement on $\vec{x}$. On the contrary, if the estimated altitude is lower than the real one, the cell will undergo a lower DEP force and consequently a smaller displacement on $\vec{x}$. It results that the feedback information on the displacement along the $\vec{x}$ axis also contains information on the altitude of the cell. The observer is based on a study of the local evolution of the DEP force along the altitude. Considering a position $\mathbf{X}^c = \begin{bmatrix} x^c & y^c \end{bmatrix}^T$, a desired position $\mathbf{X}^{des}$ and one set of voltages $\mathbf{U}$ that should displace the particle from $\mathbf{X}^c$ to $\mathbf{X}^{des}$, the FSM is used to compute the evolution the DEP force along the $\vec{x}$ axis for different altitude close to y^c. The computed values of DEP force are then used to compute the estimated induced displacement, δx, as a function of an error of the altitude. To perform statistics analysis on a relevant set of data, 3 preliminary experiments were conducted on cells, with limitation of $|E|$. 240 different sets of voltages $\mathbf{U}$ were extracted and used to study the change of the DEP force, computing by the FSM, depending on the altitude for different desired displacements $\delta\mathbf{X}^c$. The result of the study is presented in Fig. 6. The figure represents the variation of $\frac{\delta x - \delta x^c}{\delta x^c}$

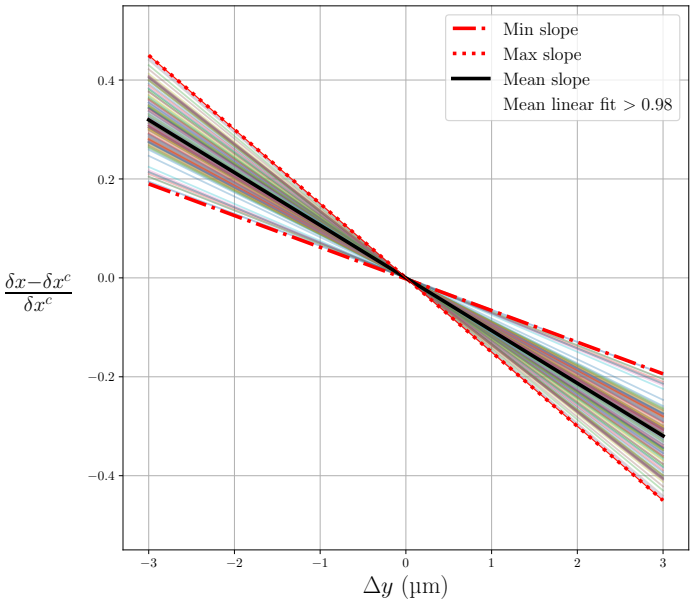

Fig. 6 The figure represents the link between an error of the estimated altitude Δy and a ratio of the error between the computed δx and desired displacement δx^c on the $\vec{x}$ axis. There is on the figure a total of 240 curves form 3 different experiments. Each curve represents the variation of displacement, compared to the desired one, as a function of the variation of the altitude for a fixed set of voltages $\mathbf{U}$ and position x. As an example, considering curve of slope sl, if the estimated altitude is correct, $\Delta y = 0$ μm, the displacement of the cell δx should be δx^c thus $\frac{\delta x - \delta x^c}{\delta x^c} = 0$. However, if $\Delta y = 1$ μm, it will induce an error of displacement of the cell of $\delta x^c \cdot sl \cdot \Delta y$. The figure reveals that the ratio $\frac{\delta x - \delta x^c}{\delta x^c}$ linearly changes with the error of altitude with a mean slope $sl_{mean} = -0.11$.

as a function of an error on the estimated altitude Δy. It shows that around the cell $\Delta y \in [-3,3]\mu$m, this variation can be represented by a linear approximation as the mean linear fit score of the 240 data set is above 0.98. In addition, the slope of those lin-

ear fit $sl \in [-0.095, -0.15]$ with $sl_{mean} = -0.11$. This study is used to establish the following model.

$$\frac{\delta x - \delta x^c}{\delta x^c} = \Delta y \cdot sl_{mean} \tag{16}$$

The goal of the observer is to correct the estimated altitude using the measured error $(\delta x - \delta x^c)$ on $\vec{x}$. It uses the model presented in section 2 to estimate the theoretical displacement from **U** and compared it to the measured one to obtain $(\delta x - \delta x^c)$. Then, the controller acts as a proportional controller on the estimated altitude $\tilde{y}$ with a gain K_p^{corr}. Knowing δx and δx^c Eq. 16 is used to compute Δy, resulting in

$$\tilde{y}^{corr} = \tilde{y} + \frac{K_p^{corr}}{sl_{mean}} \left(\frac{\delta x - \delta x^c}{\delta x^c} \right) \tag{17}$$

A simulation of the effect of this observer is presented in Supplementary materials Fig. S4. The next section describes the image processing to measure the position of the cell on the $\vec{x}$ axis.

4.2 Estimation of the position of the cell on the plan of the electrodes

The feedback information regarding the position of the cell on the $\vec{x}$ axis is obtained with image processing. A region of interest is defined in the image to reduce the computing time. The cells inside this region of interest are detected using a threshold algorithm and a blob detection one. The cell is then tracked over time. To ensure the control and avoid taking into account wrong detection, a threshold on the distance between two consecutive detection is used. If this threshold is exceeded, the measured position is ignored and an estimated position reconstructed with the model is used.

5 Materiel and methods

5.1 Experimental platform

5.1.1 Hardware

The experimental test bench is presented in Fig. 7. This setup is situated in a temperature, pressure and humidity controlled room with filtered air to ensure a "dust free" environment. A Biological Safety Cabinet - BSC (MSC advantage from Fisher scientific) is also used to manipulate cells inside a sterilized environment. The whole experimental platform is handled by a computer (Dell T3400) with OpenSuse 13.2 operating system, and a kernel 2.6 patched with RTAI 3.8.1 to achieve real time performances. This computer communicates with all the hardware and process all the data through a software developed in C++. It processes the images received from a camera (Photon Focus MV-D 1024) with a pixel size of s_{pix} =0.8 μm . It generates DC current through NI PCI 6733 analog output devices. The DC signal generated is then multiplied with a signal of reference 1 V_{rms} at a frequency f_{Hz} =50 kHz generated by a HAMEG HM8131-2 using a home-made electronic card. The output of this last electronic board is **U**, a set of sixteen AC signal independently controlled in amplitude. A SAMTEC MB1 mini edge card connector is used as a bridge between the electronic board and the microfluidic chip. A pool made of PDMS (Polydimethylsiloxane), with a thickness

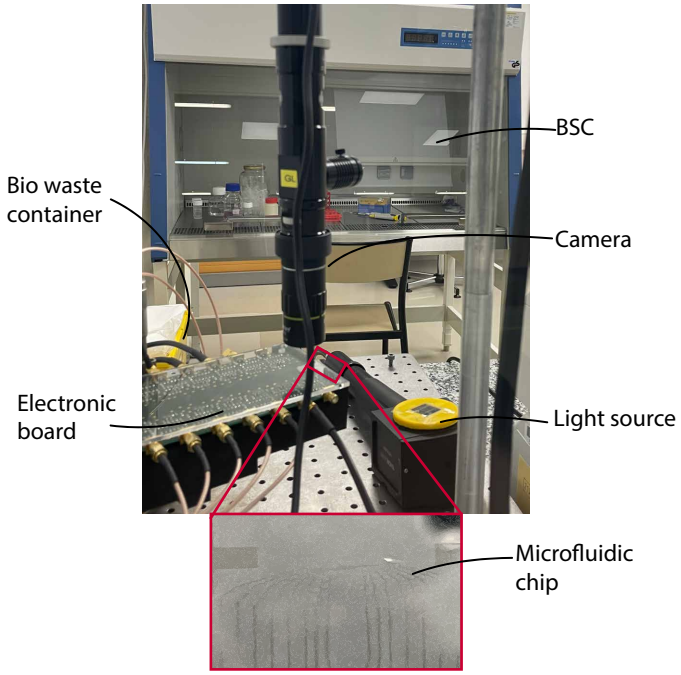

Fig. 7 Presentation of the experimental setup. It is composed of a BSC and a bio waste container to safely manipulate cells. A computer with a real time OS that is connected to a camera for visual feed-back, and to an electronic board to generate 16 independent AC signals. The microfluidic chip is connected to the electronic board and is enlightened from below.

around 1 mm is added on top of the chip and stuck by adhesion. The walls created by this pool are far from the working area and do not have an effect on the displacement of the cell. The chip details are given in the next section.

5.1.2 Microfluidic chip

The microfluidic chip is composed of 16 parallel electrodes. In our case, the cells are on top of the electrodes. With artificial objects the detection can be performed using a combination of transmission and reflection enlightenment even on top of non-transparent electrodes. However, the optical properties of the cell requires the use of transparent conductive material for the electrodes to enable the detection through image processing on top of electrodes (Fig. S3 in supplementary materials).

The chosen conductive transparent material is ITO (Indium Thin Oxide). 370 nm of ITO (Indium Thin Oxide) is deposited by the company SOLEMS on a glass BF33 wafer. This layer is then protected using a S1813 resin patterned using photo-lithography. The unprotected ITO is etched with a RIE using Argon gas only. The obtained chip is composed of electrodes with a width of 10 μm and a gap between two electrodes of 10 μm as well. The workspace is 310 μm long along the $\vec{x}$ axis.

5.2 Biological cells

Mammalian cell line CEM/C1 (CRL-2265™, ATCC®) is used. CEM/C1 is a type of human T leukemia cell line. CEM/C1 cells were grown in RPMI 1640 medium (72400-021, Gibco) supplemented with 10% fetal bovine serum (10270, Gibco) and 1% penicillin/streptomycin (15140-122, Gibco) in a humidified incubator

Table 1 Composition of the used buffer

Components	Buffer 1 : Control	Buffer 2 : Viability test
Glucose (μg mL^{-1})	11	11
Sucrose (mg mL^{-1})	104	104
RPMI (%)	13 (v/v)	13 (v/v)
BSA (%)	0.0033 (w/v)	0.0033 (w/v)
Trypan Bleu (%)	-	0.02

at 37°C in 5% of CO2. Cells were prepared at the concentration of 1.10^7 cell/mL in RPMI 1640 medium only.

A homemade buffer suited for dielectrophoretic actuation is then prepared. It is inspired from R. Di Martino *et al.*[37] and modified to reach a conductivity of $0.2\,\mathrm{S\,m^{-1}}$ while keeping the osmolarity of RPMI. The composition of the buffered is defined in Table 1 where the columns define the proportion of each component for each medium. Two buffers are prepared, "Buffer 1" is used for control trajectory experiments and "Buffer 2" is used for control trajectory followed by viability tests as it includes trypan blue.

5.3 Experimental protocol

For each experiment, the microfluidic chip surface is activated using BSA for 15 min and is then flushed, sterilized using absolute ethanol and brought under the BSC. The cells are moved into a buffer whose composition is detailed in Table 1 to reach a concentration of 1.10^6 cell/mL. $40\,\mu$L of this solution is poured into the PDMS pool and a cover glass is added at the top of the pool to seal it, to avoid leakage and to obtain a smooth surface to enable observation with the camera. The microfluidic chip is then plugged into the SAMTEC connector.

To perform viability tests, 10% of trypan blue 0.2 is added to the medium for experiments dedicated to the study of viability ("Buffer 2" in Table 1). It allows the detection of dead cells after the experiment without the need to extract the cells from the pool. This quantity of trypan blue has been determined after a study on the minimum concentration required to have an effective test. Its impact on dielectrophoresis has been checked and is negligible.

6 Results and discussion

This section presents the results obtain while controlling T-lymphocytes along three different trajectories using the method and parameters presented previously. The shape of the trajectories is chosen to study the behavior of the controller with respect to stability, precision, repeatability and acceleration. For all the curves in Fig. 8, the dotted blue curve is the measured position of the cell during the experiment while the crossed orange one is the reference trajectory. The dashed curve is the error between the two previously defined curves. The error between the measured x_k^m and the desired position x_k^{des} is called δx_{traj}. The duration of each experiment is 15 s, the desired altitude is $y^{des} = 15\,\mu$m and remains constant during all the experiments to keep the cell in the focal plan.

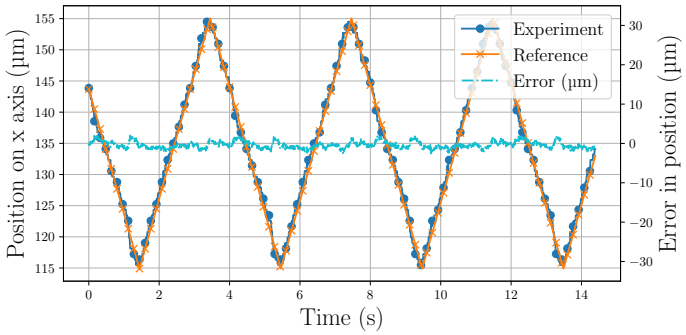

(a) Experimental result of the control of the trajectory of a T-cell along a saw shape trajectory. The orange curve is the reference path, the blue curve is the measured one during the experiments. The cyan one is the measured error of position. The maximum error during this experiment is below $4\,\mu$m

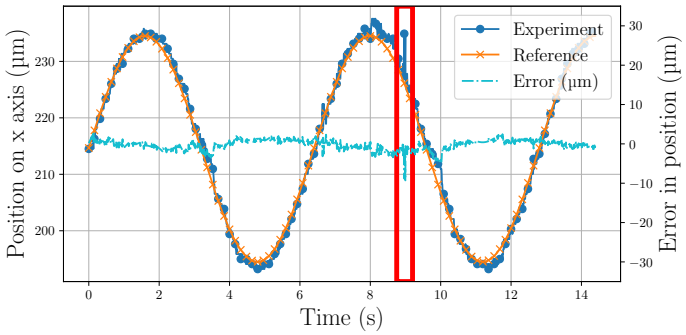

(b) Experimental result of the control of the trajectory of a T-cell along a sinusoidal shape trajectory. The orange curve is the reference path, the blue curve is the measured one during the experiments. The cyan one is the measured error of position. The point inside the red rectangle represents a wrong detection of the cell during the image processing. The fact that it has no impact on the trajectory demonstrates the efficiency of the strategy described in section 4.2 to handle such issues. The maximum error during this experiment, excluding the error of detection, is below $5\,\mu$m.

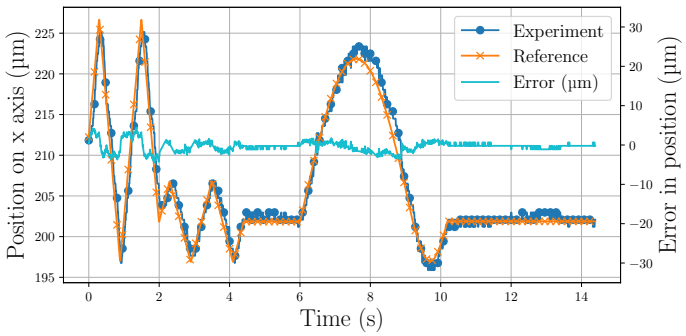

(c) Experimental result of the control of the trajectory of a T-cell along a complex trajectory. The orange curve is the reference path, the blue curve is the measured one during the experiments. The cyan one is the measured error of position. The maximum error during this experiment is below $4\,\mu$m

Fig. 8 Results of different experiments of trajectory control of T-lymphocytes. The maximum error during those experiments was below half of the diameter of the cell.

6.1 Saw shape trajectory

The first trajectory is a saw shape with a slope of $\pm 20\,\mu\mathrm{m\,s^{-1}}$. It has been performed using medium 1. The result of this experi-

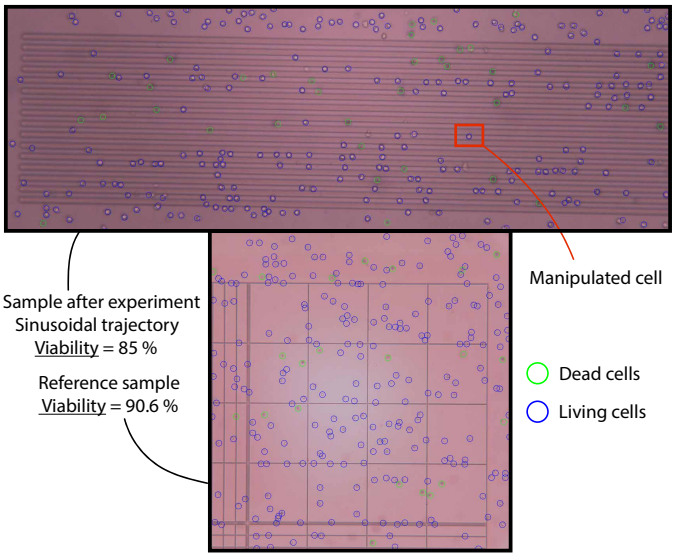

Fig. 9 Viability test of T-lymphocytes after the experiment presented in Fig. 8a. Before the experiments, the solution with cells in medium 2 was divided in two parts. One undergoes dielectrophoretic manipulation while the other one is used to fill a Malassez counting cell. After the experiment, a counting is performed on both samples on 250 cells. It results that the manipulated cell is unharmed and that the global difference of viability is 5.5%

ment is presented in Fig. 8a. The instantaneous change of direction in this trajectory shows that the inertia of the cell is negligible at this scale. The ramps show the capability of the system to move a cell with a constant speed which is directly linked to its ability to generate a same force at different locations. It is thus a way to test the precision of the control. The maximum measured error for this trajectory $\delta x_{traj}^{max} = 2.1\mu$m.

6.2 Sinusoidal shape trajectory

The second trajectory is a sinusoidal shape trajectory. This trajectory is used to demonstrate the resolution of the system being the minimum speed induced to a cell. It results that the camera is a limiting factor as the measured resolution is just below the size of a pixel of the camera used to measure the position, which is $s_{pix} = 0.8\mu$m. The result of the experiment is presented in Fig. 8b. The red square represents an error of detection that occurred during the image processing. The fact that it has no impact on the trajectory demonstrate the efficiency of the strategy described in section 4.2 to handle such issues. The mean and maximum error of trajectory during this experiment are $\delta x_{traj}^{mean} = 1\mu$m and $\delta_{traj}^{max} = 4.7\mu$m excluding the error of detection. This experiment was performed in the Medium 2 and viability test was done after the trajectory control. The result of the test is presented in Fig. 9. Before the experiments, the solution with cells in medium 2 was divided in two parts. One undergoes dielectrophoretic manipulation while the other one is used to fill a Malassez counting cell. After the experiment, a counting is performed on both samples on 250 cells. It results that the displaced cell is unharmed and that the global difference of viability is 5.5%.

6.3 Complex trajectory

The last trajectory is a combination of saw shape and sinusoidal trajectories and time of hold in position. This trajectory is used to demonstrate the capability of the system to steer cells along complex trajectories for a certain amount of time, at low and null speed as well as relatively high speed ($50\,\mu\mathrm{m\,s^{-1}}$). For this experiment the maximum error is $\delta_{traj}^{max} = 4.5\mu$m, which remains below half of the diameter of the cell. Simulation of this experiment was done to assess the observer and is presented in supplementary materials Fig. S4

6.4 Discussion

The experimental bench to study automatic trajectory control of cells using dielectrophoresis allows the control of cells along different trajectories in 2D, the direction perpendicular to the electrodes and the altitude. Those experiments have been realized inside a PDMS pool to demonstrate the importance of the altitude of the cell while using dielectrophoretic actuation. The different experiments reveal the efficiency of the observer to estimate the altitude of the cell. The T-lymphocyte are controlled along a defined path with a maximum error of half their diameter at a maximum speed of 5 time their diameter per second. This control is performed without harming the controlled cell. The errors observed during the experiments can have several causes. The inverse model used to compute the vector $\mathbf{U}$ uses parameters that are approximations of the real ones. This can lead to approximations on the estimated position. In addition, the simulated annealing algorithm, on which is based the inverse model, is an optimization algorithm that outputs the vector $\mathbf{U}$ that limits the most the error among a limited number of solutions computed in a limited number of iterations. This is a constraint due to in-line processing. Plus, the information used as a feed-back is an image whose resolution is $0.8\,\mu$m per pixel. Performing image processing on this image induces approximations regarding the measured position of the cell. The speed remains limited as $50\,\mu\mathrm{m\,s^{-1}}$ is the maximum speed that can be reached with this controller. Above this speed, the precision decreases and the control is not guaranteed. The inverted model has to find an optimal set of voltages $\mathbf{U}$ that generates a high force on the $\vec{x}$ axis and a small one on $\vec{y}$. The difference of magnitude between the generated force on the $\vec{x}$ axis and $\vec{y}$ axis increases with the targeted speed, and the number of solutions decreases. In the case of cells, the dielectrophoretic force needed on $\vec{y}$ to counter the gravity and the buoyancy is low, with a magnitude of $7e^{-13}$N. The algorithm doesn't manage to find a solution that generates this force on $\vec{y}$ and a much bigger one on $\vec{x}$, with a magnitude above $7e^{-11}$N, in the limited number of iterations. The use of the controller and model presented in this article can be extended to several applications. Inside a microfluidic channel, it can be used to automatically position cells inside the channel to create virtual ones. As the model is computed online, it can be used to perform controlled and automatic electroporation of cells. To reach higher speed of manipulation, it is necessary to have a better control and estimation on the altitude of the cell. The different behaviors of cells observed through experiments can be used to perform a statistical analysis to esti-

mate more accurately the perturbations and inaccuracies inside the model to improve the simulations. More realistic simulations could become a tool to optimize the controller. Future work will focus on the development of a microfluidic chip with parallel electrodes on top and bottom plates perpendicular to each other. This configuration will allow 3D manipulation of cells at higher speed because of the possibility to generate high electric field gradient at the top of the chip. Future work will also focus on the use of impedance spectroscopy to measure the position of the cell and perform closed loop actuation based on impedance feed-back. Beside these results, this work presents the methodology to perform automatic closed loop control of the trajectory of single cells and open the door to applications where single cell characterization is required.

7 Conclusions

This article proposes a platform based on dielectrophoretic actuation to study the control of cell trajectories. The platform allows to monitor the position of the cell, and to control in real time the electric field and dielectrophoretic force at a precise location. It is used to steer cells along a defined trajectory taking into account their physiological properties. The platform is based on a closed loop controller using visual feed-back and limiting the electric field applied to the cells. As the images are taken from a top view, the altitude of the cell is reconstructed with the model and corrected with an observer. The controller is able to run at 120 Hz. This platform is used to steer T-lymphocytes along a defined complex trajectory with a maximum speed of $50\,\mu\mathrm{m\,s^{-1}}$, a maximum error of $4.4\,\mu$m and a mean error of $1.5\,\mu$m which is approximately a tenth of the diameter of the displaced cell. Viability tests demonstrate that this trajectory control does not damage the cells and can thus be promising for more complex tasks.

Conflicts of interest

"There are no conflicts to declare".

Acknowledgements

This work has been supported by the EIPHI Graduate School (contract ANR-17-EURE-0002), by the Bourgogne Franche-Comté region through the ConAFlu project, by French RENATECH network and its FEMTO-ST technological facility and by the French ROBOTEX network and its Micro and Nanorobotics center under Grant ANR-10-EQPX-44-01, by the MiMedi project funded by BPI France under Grant DOS0060162/00, by the European Union through the European Regional Development Fund of the Region Bourgogne-Franche-Comté under Grant FC0013440. The authors would like to thank all the people indirectly involved in the project, Emma Schenckbecher specifically.

Supplementary materials

Transmembrane potential as a function of the electric field magnitude

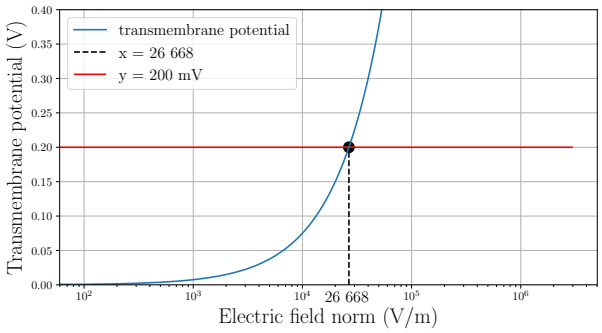

Fig. S1 Evolution of the transmembrane potential as a function of the norm of the electric field using equation 1. The simulation is done considering a human T-cell of $10\,\mu$m of diameter, $C_{mem} = 10e^{-3}\ \mathrm{F\,m^{-2}}$, $\sigma_{cyto} = 0.65\,\mathrm{S\,m^{-1}}$, $\sigma_{mem} = 20\,\mathrm{S\,m^{-1}}$ inside a medium with $\sigma_m = 0.2\,\mathrm{S\,m^{-1}}$. The horizontal line represents the maximum value of $V_{tm} = 200\mathrm{mV}$ that can be applied to avoid damaging the cells. It shows that this value corresponds to a norm of the electric field $|\mathbf{E}|_{max} = 26668\,\mathrm{V\,m^{-1}}$.

Comparison of the electric field computed by Comsol and FSM

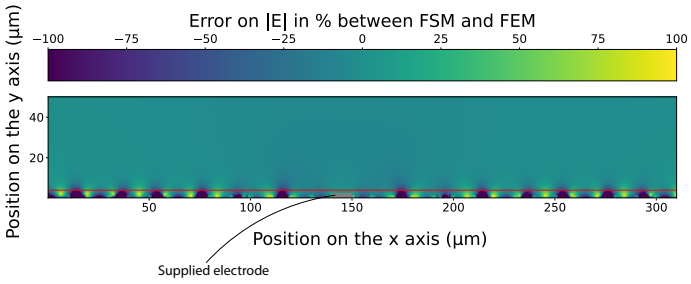

Fig. S2 Comparison of the norm of the electric field in % between the FEM and FSM model. The horizontal red line shows the limit of $5\,\mu$m. The color map represents the percentage of difference between both models. A negative value (area in purple) means that the FSM is overestimating $|E|$, a positive value (area in yellow) means that the FSM is underestimating $|E|$. Close to the supplied electrode, at $5\,\mu$m the error is between $[-20, 20]\%$, above $5\,\mu$m, the FSM is always overestimating $|E|$.

Comparison of images of cells on top of ITO and gold electrodes

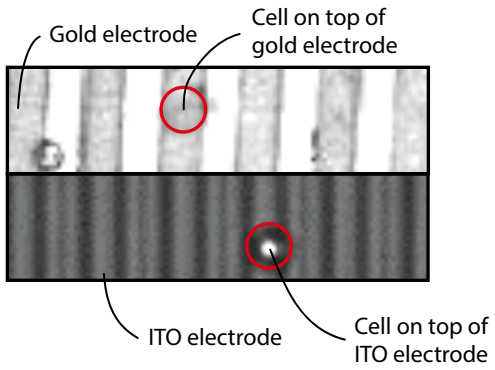

Fig. S3 Comparison of images of a cell on top of gold and ITO electrodes. The cells are inside the red circle. The cell on the top part of the image is hardly visible, the image is not usable for tracking the cell. The bottom image shows that a cell on top of ITO electrodes still has a bright inner part and can be tracked using image processing.

Effect of observer through simulation

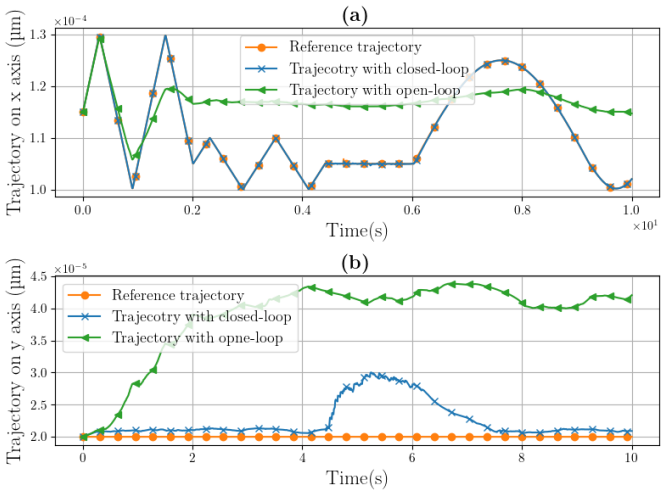

Fig. S4 Effect of the observer demonstrated through simulation. The simulation considers inaccuracies on parameters of the cell. The diameter is overestimated by 20% and the density is also overestimated by 10%. The doted curve represents the trajectory of reference which is the same as the one used in the experiment Fig. 8c. The curve with cross represents the one simulated with the closed-loop controller. The curve with triangle represents the one simulated in open-loop. Figure (a) represents the trajectory on the $\vec{x}$ axis and figure (b) represents the trajectory followed on the $\vec{y}$ axis.

References

1 Q. Huang, S. Mao, M. Khan and J.-M. Lin, *The Analyst*, 2019, **144**, 808–823.

2 T. Luo, L. Fan, R. Zhu and D. Sun, *Micromachines*, 2019, **10**, 104.

3 H. Wang, F. Zhou, Y. Guo and L. A. Ju, *European Biophysics Journal*, 2022, **51**, 119–133.

4 C. Dai, Z. Zhang, Y. Lu, G. Shan, X. Wang, Q. Zhao, C. Ru and Y. Sun, *IEEE Transactions on Robotics*, 2020, **36**, 271–283.

5 B. Ahmad, A. Barbot, G. Ulliac and A. Bolopion, *IEEE/ASME Transactions on Mechatronics*, 2022, **27**, 4090–4100.

6 Q. Jin, Y. Yang, J. A. Jackson, C. Yoon and D. H. Gracias, *Nano Letters*, 2020, **20**, 5383–5390.

7 T. D. Nguyen, Y. Q. Fu, V.-T. Tran, A. Gautam, S. Pudasaini and H. Du, *Sensors and Actuators B: Chemical*, 2020, **318**, 128143.

8 P. Li and Y. Ai, *Analytical Chemistry*, 2021, **93**, 4108–4117.

9 S. Kumar, M. Gunaseelan, R. Vaippully, A. Kumar, M. Ajith, G. Vaidya, S. Dutta and B. Roy, *Biomedical Optics Express*, 2020, **11**, 3555.

10 E. Gerena, F. Legendre, A. Molawade, Y. Vitry, S. Régnier and S. Haliyo, *Micromachines*, 2019, **10**, 677.

11 V. Varmazyari, H. Habibiyan, H. Ghafoorifard, M. Ebrahimi and S. Ghafouri-Fard, *Scientific Reports*, 2022, **12**, 12100.

12 Y.-C. Kung, K.-W. Huang, W. Chong and P.-Y. Chiou, *Small*, 2016, **12**, 4343–4348.

13 H. Yun, K. Kim and W. G. Lee, *Biofabrication*, 2013, **5**, 022001.

14 A. Salari, M. Navi, T. Lijnse and C. Dalton, *Micromachines*, 2019, **10**, 762.

15 C. Honrado, P. Bisegna, N. S. Swami and F. Caselli, *Lab on a Chip*, 2021, **21**, 22–54.

16 H. Zhang, H. Chang and P. Neuzil, *Micromachines*, 2019, **10**, 423.

17 N. Godino, F. Pfisterer, T. Gerling, C. Guernth-Marschner, C. Duschl and M. Kirschbaum, *Lab on a Chip*, 2019, **19**, 4016–4020.

18 M. Di Trapani, N. Manaresi and G. Medoro, *Cytometry Part A*, 2018, **93**, 1260–1266.

19 F. Lessi, S. Franceschi, M. Morelli, M. Menicagli, F. Pasqualetti, O. Santonocito, C. Gambacciani, F. Pieri, F. Aquila, P. Aretini and C. M. Mazzanti, *Cells*, 2022, **11**, 1127.

20 P. D'Amico, C. Reduzzi, W. Qiang, Y. Zhang, L. Gerratana, Q. Zhang, A. A. Davis, A. N. Shah, M. Manai, G. Curigliano and M. Cristofanilli, *Cancers*, 2021, **14**, 79.

21 M. Vismara, C. Reduzzi, M. Silvestri, F. Murianni, G. Lo Russo, O. Fortunato, R. Motta, D. Lanzoni, F. Giovinazzo, P. Miodini, S. Pasquali, P. Suatoni, U. Pastorino, L. Roz, G. Sozzi, V. Cappelletti and G. Bertolini, *Clinical Chemistry*, 2022, **68**, 691–701.

22 J. Zemánek, T. Michálek and Z. Hurák, *Lab on a Chip*, 2018, **18**, 1793–1801.

23 M. Kharboutly and M. Gauthier, 2013 IEEE International Conference on Robotics and Automation, Karlsruhe, Germany, 2013, pp. 1446–1451.

24 T. Michálek, A. Bolopion, Z. Hurák and M. Gauthier, *Physical Review E*, 2019, **99**, 053307.

25 Vladimir Gauthier, Aude Bolopion and Michaël Gauthier, *Micromachines*, 2017, **8**, 253.

26 A. Lefevre, V. Gauthier, M. Gauthier and A. Bolopion,

IEEE/ASME Transactions on Mechatronics, 2022, **27**, 4764–4773.

27 V. L. Sukhorukov, G. Meedt, M. Kürschner and U. Zimmermann, *Journal of Electrostatics*, 2001, **50**, 191–204.

28 J. Cottet, O. Fabregue, C. Berger, F. Buret, P. Renaud and M. Frénéa-Robin, *MyDEP: A New Computational Tool for Dielectric Modeling of Particles and Cells*, Zenodo, 2019.

29 T. Batista Napotnik, T. Polajžer and D. Miklavčič, *Bioelectrochemistry*, 2021, **141**, 107871.

30 N. Mittal, A. Rosenthal and J. Voldman, *Lab on a Chip*, 2007, **7**, 1146.

31 V. Gauthier, A. Bolopion and M. Gauthier, 2018 IEEE/RSJ International Conference on Intelligent Robots and Systems (IROS), Madrid, 2018, pp. 4869–4874.

32 M. Kharboutly, M. Gauthier and N. Chaillet, *Journal of Applied Physics*, 2009, **106**, 114312.

33 A. Ambari, B. Gauthier Manuel and E. Guyon, *Journal de Physique Lettres*, 1983, **44**, 143–146.

34 A. Ambari, B. Gauthier-Manuel and E. Guyon, *Journal of Fluid Mechanics*, 1984, **149**, 235.

35 V. Nerguizian, A. Alazzam, D. Roman, I. Stiharu and M. Burnier Jr., *ELECTROPHORESIS*, 2012, **33**, 426–435.

36 M. Gurtner and J. Zemánek, *Measurement Science and Technology*, 2016, **27**, 127003.

37 R. Di Martino, M. Camarda, M. Cascio, M. Gallo, A. Magliano, S. Baldo, A. Romano, L. Minafra, G. I. Forte, G. Russo, M. C. Gilardi, F. Di Raimondo, S. Scalese and A. La Magna, *Sensing and Bio-Sensing Research*, 2016, **7**, 162–167.